

Article

A New Cable-Driven Model for Under-Actuated Force–Torque Sensitive Mechanisms

Giovanni Gerardo Muscolo *  and Paolo Fiorini 

Altair Robotics Laboratory, Department of Engineering for Innovation Medicine, Section of Engineering and Physics, University of Verona, Ca' Vignal 2—Strada Le Grazie 15, 37134 Verona, Italy; paolo.fiorini@univr.it

* Correspondence: giovannigerardo.muscolo@univr.it

Abstract: Force–torque sensors are used in many and different domains (i.e., space, medicine, biology, etc.). Design solutions of force–torque sensors can be conceived by using many types of connections or components; however, there are only a few sensors designed using cable-driven systems. This could be related to many reasons, one of which being that cables are able only to pull and not push. In this paper, a new cable-driven model for under-actuated force–torque sensing mechanisms is proposed, simulated, and tested, underlining the novelty of using cables for force–torque sensing. Analytical formulations, simulations, and physical implementations are presented in this paper. Results confirm that the new proposed model can be used for force–torque sensing mechanisms in micro- and macro- applications where under-actuation is a fundamental requirement, as in robotic surgery. The proposed model and mechanism can be used in the design of sensors and actuators. The innovative model is validated with two different test benches, opening new challenges in the design and development of under-actuated force–torque transducers.

Keywords: cable mechanisms; cable-driven systems; force–torque sensors; micro-mechanisms; minimally invasive robotic surgery; surgical robotics; micro-electro-mechanical systems; compliant mechanisms; sensitive mechanisms; under-actuated mechanism; under-actuation; force–torque transducers



Citation: Muscolo, G.G.; Fiorini, P. A New Cable-Driven Model for Under-Actuated Force–Torque Sensitive Mechanisms. *Machines* **2023**, *11*, 617. <https://doi.org/10.3390/machines11060617>

Academic Editor: Dan Zhang

Received: 23 April 2023

Revised: 25 May 2023

Accepted: 31 May 2023

Published: 3 June 2023



Copyright: © 2023 by the authors. Licensee MDPI, Basel, Switzerland. This article is an open access article distributed under the terms and conditions of the Creative Commons Attribution (CC BY) license (<https://creativecommons.org/licenses/by/4.0/>).

1. Introduction

Nowadays, sensors are used in many different contexts and domains (i.e., space, medicine, engineering, biology, etc.), allowing users to analyse the behaviour of the systems.

Force–torque sensors are used to measure the forces and torques exchanged between two or more systems in order to define their physical interaction.

Among the possible sensor configurations, the conceptual architecture of parallel mechanisms is very useful for the design of force–torque sensors. The motion of a mobile part, connected with joints and links to a fixed part, is the core of a force–torque sensor's design. The local reference system (on the mobile part) can be moved with respect to the absolute reference system (on the fixed part). The displacement between the two reference systems is one aspect which permits the exchanged forces and torques between the two parts and their physical connections to be reconstructed to find the applied forces/torques. The types of physical connection between the two parts (mobile and fixed) have been explored by many researchers. An overview on force–torque sensors for microscopic and macroscopic applications, including the surgical robotic field, can be found in Muscolo and Fiorini [1]. One output of the review is that the force–torque sensors developed in the literature can be divided on the basis of three types of physical connections between mobile and fixed parts: rigid connections (e.g., using beams), soft connections (e.g., using cables or membranes), or no connections (e.g., using magnets). Nowadays, the most used sensors are those with rigid connections.

The Stewart platform is an example of a parallel mechanism used for its design architecture in the design and development of force–torque sensors [2]. In [3], the authors

present a review of Stewart platform manipulators, in which a mobile part is connected to a fixed part using links, spherical joints, and prismatic actuators. Sorli and Pastorelli defined the general design of a force–torque sensor, conceived with the Stewart platform architecture [4]. Many research papers have been published in which an architecture with a Stewart platform is used for force–torque sensor design. In [5], the authors use a near-singular configuration to define a force–torque sensor based on a Stewart platform. Rotary joints are replaced with flexible hinges, and strain-gauges are used as sensing elements in the developed prototype. In [6], applications in minimally invasive robotic surgery are proposed. The realized system is conceived with the Stewart platform architecture and with reduced dimensions because the mobile and fixed parts must be included in the surgical instrument with a diameter of around 10 mm. Flexural hinges are used instead of joints; six strain gauges are used as sensing elements and mounted on each of the six links of the Stewart platform. In [7], a six-component contact force measurement device is presented with a Stewart platform structure. Each of the six physical connections between mobile and fixed parts is composed of a wire connected to a strain-gauged cantilever.

Force–torque sensors can be designed using many other physical architectures, such as the one based on a Maltese Cross shape [8,9], but also in this case, the sensor can be designed with fixed and mobile parts connected by links. In the Maltese Cross shape case, the motion of the mobile part, generated by an external load, can be evaluated via the analysis of the deformation of the links positioned in the cruciform shape.

Other architectures for force–torque sensor design can be defined by using different structures (e.g.: a combination between the Stewart platform and the Maltese Cross shape). Some examples of mixed architectures can be found in [1,10–12].

Cable-driven systems [13,14] or membranes [15–17] are examples of soft physical connections which can be used as sensitive elements. Cable-driven mechanisms are used in different contexts, such as rehabilitation [18], the design of exoskeletons [19], industry [20], or in mechanical designs for general applications [21–23].

Some researchers used the pretension of fibre Bragg gratings to wrap the fibre around the mechanical transducer [24]. In [25], the authors presented a minimally invasive robotic surgery instrument in which the sensor is included in the rear part of the surgical instrument, analysing the tension of cables. Recently, researchers studied a cable-driven robotic system for aeronautical applications [26]. The differences in the cable tension are amplified to read the force sensitivity of the cables. The paper [26] underlines the advantages of using cable-driven parallel robots (CDPR) instead of rigid links parallel robots, as follows:

- Their convenient disassembly/reassembly;
- Their light-weight structures;
- Their high payload-to-weight ratios.

These three advantages are very useful in the robotic surgery research field.

In this paper, we propose a new model of a cable-driven force–torque sensing mechanism that can be used as an under-actuated force–torque sensor or actuator. The mechanism consists of one mobile part and one fixed part connected to each other by soft physical connections (e.g., using cables). The mechanism has been conceived to solve problems in the robotic surgery research field. For example, robotic tools must be sterilized for use in minimally invasive robotic surgery, and the process of sterilization is dangerous for the electronic components and sensing elements of the instrument [1]. The invention shown in this paper is a sensorized mechanism consisting of an under-actuated platform connected with cables. If this mechanism is included in a minimally invasive robotic surgery tool, the part of the robotic tool that can be sterilized is composed of cables and a rigid structure, and the electronic part remains outside the human body and does not need sterilization. The cable-driven model and mechanism presented in this paper can be used in many different domains, as well as outside the robotic surgery field. The proposed architecture can be used as a sensor or an actuator and for micro- and macro- applications.

The paper is organized as follows: Section 2 shows the problem statement of the force feedback during robotic surgery and the proposed innovation in comparison to cable-driven

parallel manipulators; Section 3 presents the kinematic model of the proposed solution and some configurations; Section 4 shows the simulation of and comparison between two configurations; Section 5 presents the analytical formulation of the sensing mechanism; Section 6 shows the developed test bench prototypes for the experiments; Section 7 includes results and discussion. The paper ends with the conclusions and future research directions.

2. Problem Statement and Proposed Solution

2.1. Da Vinci Robotic Tools (dVRTs)

The da Vinci Robot is a Minimally Invasive Robotic Surgery (MIRS) system, developed by Intuitive Surgical, Sunnyvale, CA, USA [1]. It is composed of two parts, located in two different places and connected by tele-operation:

- Local part: located near the surgeon and controlled directly by the hands of the surgeon;
- Remote part: located near the patient and tele-operated by the local part.

The local part does not give force feedback to the surgeon but permits them to control the remote part (in open-loop) using only a vision system. The remote part consists of the da Vinci Robotic Arms (dVRAs) and da Vinci Robotic Tools (dVRTs) or Minimally Invasive Robotic Tools (MIRTs), as shown in Figure 1 [1].

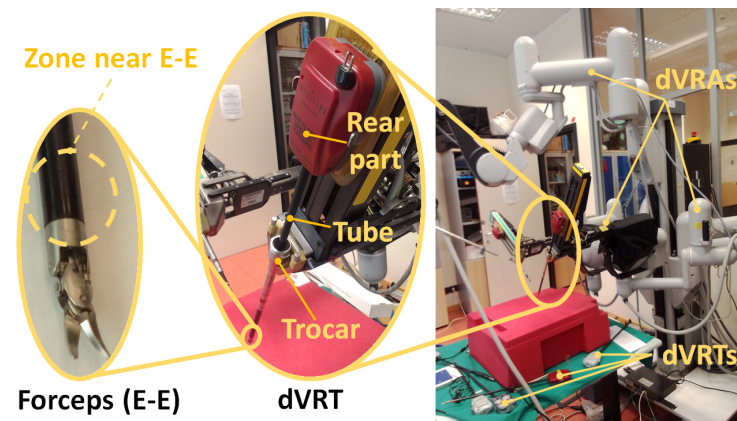


Figure 1. Remote part of the da Vinci Robotic Kit (dVRK) constituted by da Vinci Robotic Tools (dVRTs) and da Vinci Robotic Arms (dVRAs). Courtesy of the Altair Robotic Lab, University of Verona.

The dVRT is composed of a rear part (assembled on the robotic arm), a tube, and an End-Effector (E-E), constituted by forceps, or other systems used for MIRS. The dVRT uses cable-driven mechanisms to move the forceps [1]. Cables passing inside the tube connect the E-E to the pulleys in the rear part.

During MIRS operations, the dVRT is forced to pass through a trocar (see Figure 1), i.e., a connection and separation system between the external environment and the interior of the human body. All tools in contact with the human body must be sterilized.

2.2. Problem Statement: Force Feedback in Robotic Surgery

In order to give force feedback to the surgeon (via the local part of the robot), many solutions were proposed [1]. One of the desirable solutions is the inclusion of sensitive elements in the surgical instrument (on the remote part). This solution is not simple to implement because many constraints should be considered. One of these constraints is to develop a sensor able to resist the routine sterilization process at high temperature.

Many research solutions proposed the implementation of sensitive elements in the rear part of the surgical instrument [25,27–29], or on the robotic arm [30]. This approach is good because it allows the sterilization of the sensor to be avoided (because it is not near the E-E). However, the signals of the sensor are corrupted by many disturbances, amplified by the connections between the E-E (of the surgical instrument) and the robotic arm.

Other solutions include an added sensitive element near the E-E of the tool (see zone near E-E, Figure 1) [6,31,32]. In this case, the errors in the signal data of the sensor are reduced, but problems emerge during the sterilization process of the electronic components.

2.3. Proposed Solution: Cable-Driven Force–Torque Sensing Mechanism

We thought to use cable-driven systems, also used in the dVRT for the actuation of the E-E, to design our force–torque sensitive mechanism. The under-actuation of cables is convenient in robotic surgery, since it allows direct contact between the electronic part and the sterilized zone of the surgical instrument to be avoided. In the proposed solution in this paper, we tried to merge the advantages of the two approaches presented above: we include the sensitive mechanism near the E-E of the tool (reducing gap errors in the signal data) and the electronic components of the mechanism outside of the sterilizing zone (thanks to the cable connections and avoiding the sterilization of the electronic part).

Some innovations of the cable-driven sensitive mechanism proposed in this paper are given below:

- Hybrid System: the mechanism can be used as a sensor and/or actuator;
- Modelling: the model of the mechanism is constituted by an external mobile part connected with cables to an internal fixed structure;
- Application: micro- and macro- applications can be performed with the proposed mechanism;
- Under-actuation: the mechanism is composed of a cable-driven, under-actuated system.

2.3.1. Hybrid System: Sensor and/or Actuator

The proposed solution in this paper allows devices to be created which can be used as sensors or actuators, respectively measuring forces from the environment or implementing forces on the environment.

In its general form, our solution is composed of two elements, A and B, as shown in Figure 2, divided by a C zone. Element A can interact with the external environment as a sensor (measuring force resultants) or as an actuator (acting force resultants). Element A can be stationary or in motion with respect to the fixed element B. The C zone can be constituted by different types of elements or connections between A and B: membranes, cables, tendons, magnets, etc. Based on the deformation or displacement of the elements in C, the forces on A (when used as a sensor) or from A (when used as an actuator) can be determined.

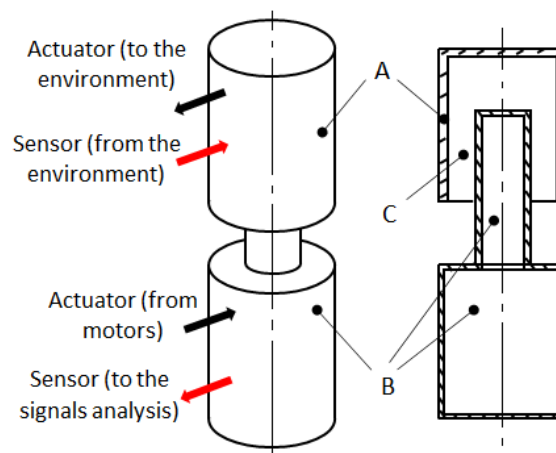


Figure 2. General scheme of the working principle of the invention: trigonometric view (on the left) and section (on the right). Element A can be stationary or in motion with respect to the fixed element B. The C zone can be constituted by different types of elements or connections between A and B: membranes, cables, tendons, magnets, etc.

In this paper, the mechanism is used as a sensor, using cables in the C zone.

2.3.2. Modelling: An Internal Cable-Driven Fixed Structure

The classical model used to describe CDPR is composed of an external parallelepiped connected to an internal parallelepiped using cables (pulleys are approximated to points) [21–23,26]. The fixed and mobile parts are the external and the internal parallelepipeds, respectively. The motion of the internal parallelepiped is calculated with respect to the external one by using screw theory [7], or other analytical methods, and computing the tension of the cables.

In order to integrate our solution in the cylindrical tube of the surgical instrument (with a tube diameter of around 10 mm, see Figure 1), it is convenient to conceive different models, in which the mobile part (A) is external and the fixed part (B) is internal. Cables can pass inside the fixed part to connect B to A. We simplified the classical model with parallelepipeds using the cylindrical symmetry of the system.

Figure 3 shows two cylindrical configurations of our cable-driven mechanism. The two presented configurations will be analysed in detail in the following sections and represent the two extreme conditions in which the length of part B (b_i) is shorter or longer than the length of part A (a_i):

$$b_{min} < b_{iI} < a_{max} \tag{1}$$

$$a_{min} < b_{iII} < b_{max} \tag{2}$$

where b_{iI} and b_{iII} are the lengths of the internal cylinder (part B) in the two configurations I and II; a_i is the length of the external cylinder (part A); a_{max} , b_{max} , a_{min} , and b_{min} are the maximum and minimum values of the height of the two cylinders; and D_A and D_B are the diameters of the mobile (A) and fixed (B) cylinders, respectively.

Another condition to be respected is the following one:

$$D_A > D_B \tag{3}$$

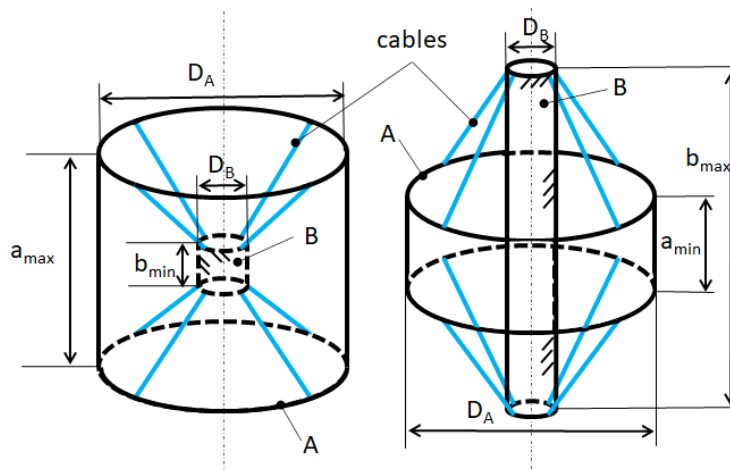


Figure 3. Two configurations used for the cable-driven mechanism: configuration I (on the left) and configuration II (on the right). Part A is the mobile part and part B is the fixed part.

2.3.3. Application: Micro/Macro Cable-Driven Applications

From the application point of view, the model has been conceived for micro- applications (e.g., containing the system in a minimum cylinder of 10 mm diameter). However, macro-applications can be found in different contexts and domains. This point can be considered as an open challenge.

Figure 4 shows an example of the implemented configurations on the tube of the surgical instrument. The analysis of the tension of eight cables allows the external resultant forces on the mobile part A to be defined.

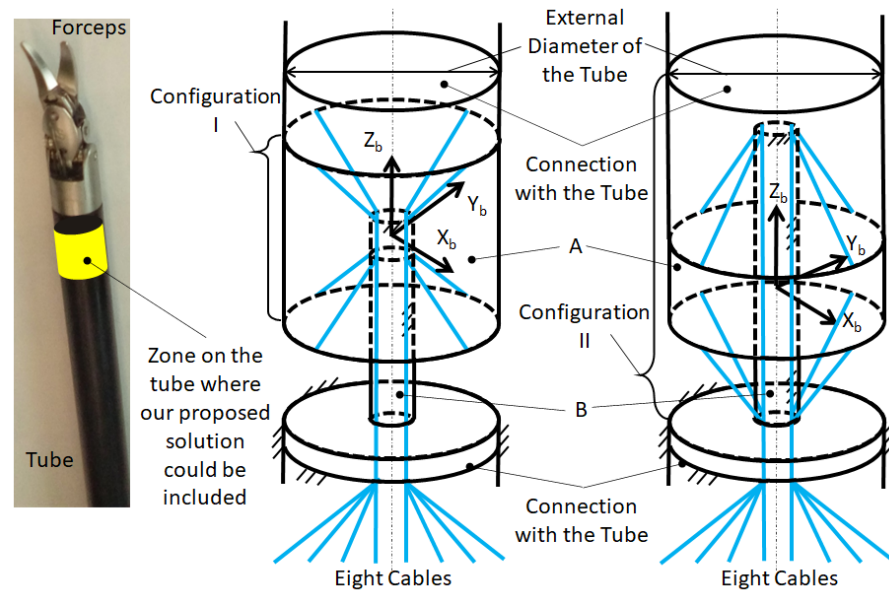


Figure 4. Example of implemented configurations on the tube of the surgical instrument. Part A is the mobile part and part B is the fixed part.

2.3.4. Under-Actuation: Cable-Driven System

The under-actuation allows the use of a light system and separates the zone of motion of the mobile part from the zone of the electronics part and the sensor’s implementation. This is very convenient in robotic surgery, bypassing the sterilization problem related to the use of electronic components. The under-actuation also allows more accurate sensors to be used because in the rear part of the instrument, minor constraints on dimensions, permeability, and other features are required.

3. Analysis of the Mechanism’s Configurations

3.1. Details of the Kinematic Model

Figure 5 shows the two reference systems on the fixed B ($O_B - X_B Y_B Z_B$) and mobile A platforms ($O_A - X_A Y_A Z_A$), where i is the cable number from 1 to k and j is the equilibrium positions, initial $j = 0$ and final $j = 1$. The reference system of the mobile platform A ($O_A - X_A Y_A Z_A$) is applied to its centre of mass G ($O_A = G$), and in the position $j = 0$, it is coincident with O_B . N_{Bij} , N_{Aij} , \mathbf{p}_{Bi} , and \mathbf{p}_{Ai} are the two anchor points of the cables (N_{Bij} , N_{Aij}) and their two position vectors (\mathbf{p}_{Bi} , \mathbf{p}_{Ai}), respectively; \mathbf{C}_{ij} is the vector of the cables, and \mathbf{r}_{ij} the unit vector of the cables. The position of the mobile platform A with respect to the fixed one B is shown by the vector \mathbf{p}_G . P is a general point on A, and \mathbf{p}_P and \mathbf{p}_z are the position vectors of the point P with respect to the reference systems in B (\mathbf{p}_P) and A (\mathbf{p}_z). It is possible to write the kinematic equation of the k cables in a general form, using the rotational matrix Q to transform the vectors calculated in the mobile platform A with respect to the fixed platform B:

$$\mathbf{C}_{ij} = -\mathbf{p}_{Bi} + \mathbf{p}_G + \mathbf{Q}\mathbf{p}_{Ai}; i = 1, \dots, k; j = 0, 1. \tag{4}$$

If part A is in equilibrium, the resultants of forces (\mathbf{F}) and torques (\mathbf{M}) are zero:

$$\sum \mathbf{F} = 0 = \sum_{i=1}^k \mathbf{T}_{ij} + m\mathbf{g}_G + \mathbf{F}_P \tag{5}$$

$$\sum \mathbf{M} = 0 = \sum_{i=1}^k (\mathbf{Q}\mathbf{p}_{Ai} \wedge \mathbf{T}_{ij}) + (\mathbf{p}_G \wedge m\mathbf{g}_G) + (\mathbf{p}_P \wedge \mathbf{F}_P) + \mathbf{M}_P \tag{6}$$

where $\sum_{i=1}^k \mathbf{T}_{ij} = \sum_{i=1}^k T_{ij} \mathbf{r}_{ij}$ is the tension of cables applied to the mobile platform A in N_{Aij} ; $\sum_{i=1}^k (\mathbf{Q}_{P_{Ai}} \wedge \mathbf{T}_{ij}) = \sum_{i=1}^k (\mathbf{Q}_{P_{Ai}} \wedge T_{ij} \mathbf{r}_{ij})$ is the torque produced by the cables; $m\mathbf{g}_G$ is the gravity; and \mathbf{F}_P and \mathbf{M}_P are the external forces and torques applied to the point P, respectively. In a more compact form:

$$\begin{bmatrix} \mathbf{r}_{1j} & \dots & \mathbf{r}_{kj} \\ \mathbf{Q}_{P_{A1}} \wedge \mathbf{r}_{1j} & \dots & \mathbf{Q}_{P_{Ak}} \wedge \mathbf{r}_{kj} \end{bmatrix} \begin{bmatrix} T_{1j} \\ \vdots \\ T_{kj} \end{bmatrix} = - \begin{bmatrix} m\mathbf{g}_G \\ (\mathbf{p}_G \wedge m\mathbf{g}_G) \end{bmatrix} - \begin{bmatrix} \mathbf{F}_P \\ (\mathbf{p}_P \wedge \mathbf{F}_P) + \mathbf{M}_P \end{bmatrix} \quad (7)$$

$$\mathbf{S}\mathbf{T}_j = -\mathbf{W}_G - \mathbf{W}_{Pj} \quad (8)$$

where \mathbf{S} is the force transformation matrix [5]; \mathbf{T}_j is the vector of the cables' tension; and \mathbf{W}_G is the gravity vector [26]. The vector of the external forces and torques, applied in the point P (\mathbf{W}_{Pj}), is calculated by analysing the variation in the tension of the cables $\Delta\mathbf{T} = \mathbf{T}_1 - \mathbf{T}_0$, in which \mathbf{T}_0 is the vector of the tension of the cables, used as an offset and calculated at the equilibrium condition $j = 0$:

$$\mathbf{S}\mathbf{T}_0 = \mathbf{S} \begin{bmatrix} T_{10} \\ \vdots \\ T_{k0} \end{bmatrix} = -\mathbf{W}_G - \mathbf{W}_{P0} \quad (9)$$

By the analysis of Equation (8) and using the difference between the condition $j = 1$ and $j = 0$, \mathbf{W}_{Pj} is obtained:

$$\mathbf{W}_{Pj} = [F_{PX}, F_{PY}, F_{PZ}, M_{PX}, M_{PY}, M_{PZ}]^T = \mathbf{W}_{P0} - \mathbf{S}\Delta\mathbf{T} \quad (10)$$

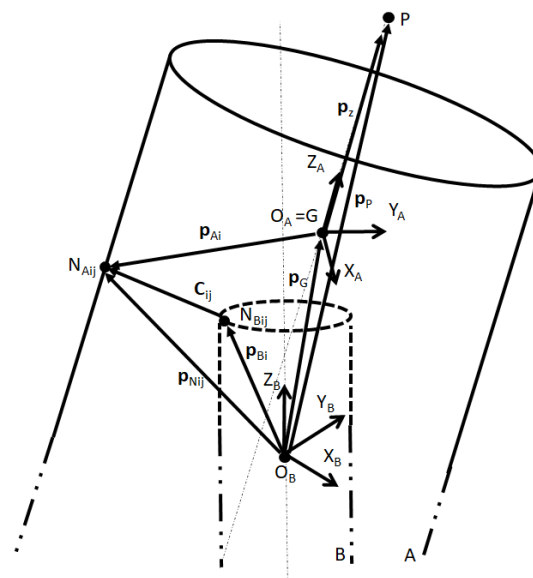


Figure 5. Sketch to determine the kinematic model of the cable-driven mechanism. A is the local reference system and B is the absolute reference system.

If the proposed cable-driven mechanism is used as a force–torque sensor, in order to increase the sensitivity of the entire system, the geometry of the mechanism must be optimised to obtain low variations in cable tension for small displacements of the mobile part A.

In line with [26], we optimise the geometrical dimensions of the two configurations of the mechanism (shown in Figure 3) to find the best solution providing more sensitivity; however, we use a different method than the one proposed in [26].

Figure 3 shows the two studied configurations. The difference between the two configurations is underlined by the different positions of cables with respect to the two parts, A and B. In configuration I, the height of cylinder B (b_{II}) is less than the height of cylinder A, as shown in Equation (1). The opposite is shown in configuration II, Equation (2), in which the height of cylinder B (b_{III}) is larger than the height of cylinder A. Part A is in equilibrium: the resultant of forces and torques are zero ($\sum \mathbf{F} = 0$ and $\sum \mathbf{M} = 0$).

Our final objective is to find the most optimised geometry for the two presented configurations in order to measure the tension of the cables. If the external forces/torques are applied to the system, the variation in the tension of the cables gives us information on the entity of the external forces/torques.

3.2. Configuration I

Figure 6 (on the left) shows a general representation of the configuration I. Thanks to the cylindrical symmetry of the entire system, the calculations can be simplified and the mechanism can be studied in the planar case. Part B is partially fixed, only allowing the rotation around the axial cylindrical axis, and part A is in equilibrium. The forces acting on part A are:

- External forces and torques in condition $j = 1$: $\mathbf{W}_{P1} = [F_{PX}, F_{PY}, F_{PZ}, M_{PX}, M_{PY}, M_{PZ}]^T$;
- Gravity: $\mathbf{W}_G = [0, 0, -mg_G, 0, 0, 0]^T$;
- Tension of cables in condition $j = 1$: $\mathbf{T}_1 = [T_{11}, T_{21}, T_{31}, T_{41}, T_{51}, T_{61}, T_{71}, T_{81}]^T$;
- Offset in condition $j = 0$: $\mathbf{T}_0 = [T_{10}, T_{20}, T_{30}, T_{40}, T_{50}, T_{60}, T_{70}, T_{80}]^T$.

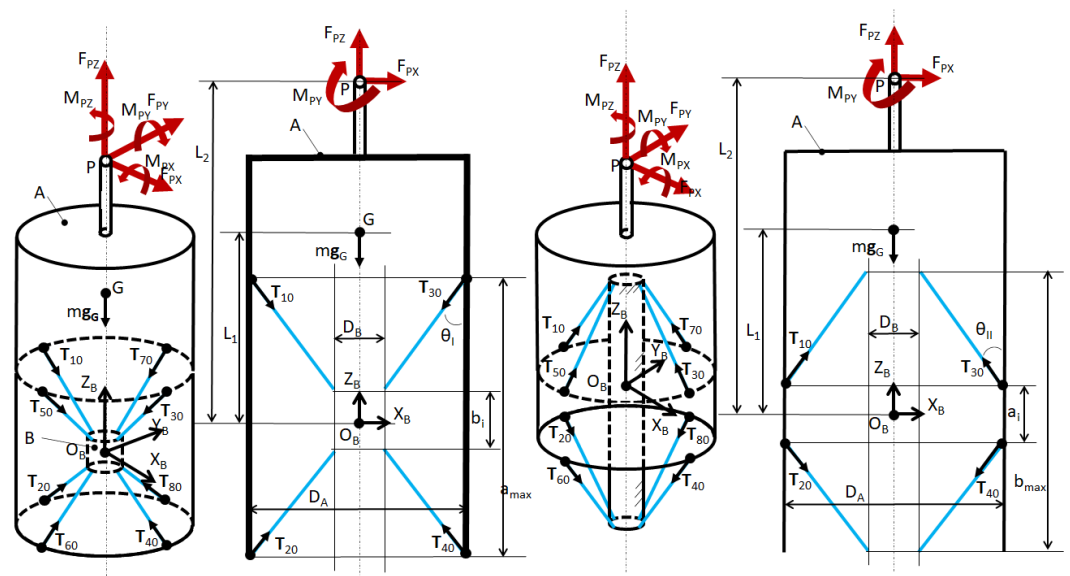


Figure 6. Configurations I (on the left) and II (on the right): spatial and planar representations. $\mathbf{W}_{P1} = [F_{PX}, F_{PY}, F_{PZ}, M_{PX}, M_{PY}, M_{PZ}]^T$ are the external applied vectors of forces and torques; $\mathbf{T}_0 = [T_{10}, T_{20}, T_{30}, T_{40}, T_{50}, T_{60}, T_{70}, T_{80}]^T$ are the vectors of the tension of the cables in condition $j = 0$.

Using the equilibrium conditions ($\sum \mathbf{F} = 0, \sum \mathbf{M} = 0$), the vector \mathbf{W}_{P1} can be determined by finding the S_I matrix for configuration I with $c\theta_I = \cos(\theta_I)$ and $s\theta_I = \sin(\theta_I)$:

$$S_{I0} = \begin{bmatrix} -s\theta & -s\theta_I & +s\theta_I & +s\theta_I & 0 & 0 & 0 & 0 \\ 0 & 0 & 0 & 0 & -s\theta_I & -s\theta_I & +s\theta_I & +s\theta_I \\ +c\theta_I & -c\theta_I & +c\theta_I & -c\theta_I & +c\theta_I & -c\theta_I & +c\theta_I & -c\theta_I \\ 0 & 0 & 0 & 0 & -h_{I0} & -h_{I1} & +h_{I0} & +h_{I1} \\ +h_{I0} & -h_{I1} & -h_{I0} & +h_{I1} & 0 & 0 & 0 & 0 \\ 0 & 0 & 0 & 0 & 0 & 0 & 0 & 0 \end{bmatrix} \tag{11}$$

where

$$h_{I0} = ((L_2 - a_{max}/2)\sin(\theta_I) + (D_A/2)\cos(\theta_I)) \quad (12)$$

$$h_{I1} = ((L_2 + a_{max}/2)\sin(\theta_I) - (D_A/2)\cos(\theta_I)) \quad (13)$$

The geometrical dimensions a_{max} , b_i , D_A , and D_B can be optimised and can be included in the angle θ_I and in the length of the cable C_I :

$$C_I = \sqrt{((a_{max} - b_i)/2)^2 + ((D_A - D_B)/2)^2} \quad (14)$$

$$\theta_I = \arctan((D_A - D_B)/(a_{max} - b_i)) \quad (15)$$

3.3. Configuration II

Figure 6 (on the right) shows configuration II, following the relative equations with S_{II} matrix for configuration II and with $c\theta_{II} = \cos(\theta_{II})$ and $s\theta_{II} = \sin(\theta_{II})$:

$$\mathbf{S}_{II0} = \begin{bmatrix} -s\theta_{II} & -s\theta_{II} & +s\theta_{II} & +s\theta_{II} & 0 & 0 & 0 & 0 \\ 0 & 0 & 0 & 0 & -s\theta_{II} & -s\theta_{II} & +s\theta_{II} & +s\theta_{II} \\ -c\theta_{II} & +c\theta_{II}a & -c\theta_{II} & +c\theta_{II} & -c\theta_{II} & +c\theta_{II} & -c\theta_{II} & +c\theta_{II} \\ 0 & 0 & 0 & 0 & -h_{II0} & -h_{II1} & +h_{II0} & +h_{II1} \\ +h_{II0} & +h_{II1} & -h_{II0} & -h_{II1} & 0 & 0 & 0 & 0 \\ 0 & 0 & 0 & 0 & 0 & 0 & 0 & 0 \end{bmatrix} \quad (16)$$

where

$$h_{II0} = (L_2 - a_i/2)\sin(\theta_{II}) - (D_A/2)\cos(\theta_{II}) \quad (17)$$

$$h_{II1} = (L_2 + a_i/2)\sin(\theta_{II}) + (D_A/2)\cos(\theta_{II}) \quad (18)$$

The geometrical dimensions b_{max} , a_i , D_A , and D_B , can be optimised and can be included in the angle θ_{II} and in the length of the cable C_{II} :

$$C_{II} = \sqrt{((b_{max} - a_i)/2)^2 + ((D_A - D_B)/2)^2} \quad (19)$$

$$\theta_{II} = \arctan((D_A - D_B)/(b_{max} - a_i)) \quad (20)$$

4. Configurations I and II: Comparison and Simulation

The elements of the two matrices (\mathbf{S}_{I0} and \mathbf{S}_{II0}) have their first three rows function according to the two angles (θ_I and θ_{II}).

Equation (10) shows that the first three rows of the matrix \mathbf{S} allow one to find the three force components (F_{PX} , F_{PY} , F_{PZ}) of the applied vector in P (\mathbf{W}_{P1}). The advantage of using one configuration over another one is not underlined by the values of θ_I and θ_{II} . If $\theta_I \rightarrow \pi/2^-$ and $\theta_{II} \rightarrow \pi/2^-$, or $\theta_I \rightarrow 0^+$ and $\theta_{II} \rightarrow 0^+$, it is possible to note that the first three rows of the matrices have the same values with the opposite signs. This means that the geometry of the configuration cannot give any other contribution to optimise the entire system.

The advantage of using one configuration instead of the other is identified by analysing the last three rows of the matrices, which allows one to find the three torque components (M_{PX} , M_{PY} , M_{PZ}) applied in P, as shown in Equation (10). The last three rows of the two matrices \mathbf{S}_{I0} and \mathbf{S}_{II0} (shown in Equations (11) and (16)) have the same forms, and the differences between the two configurations are represented by the four elements h_{I0} , h_{I1} , h_{II0} , and h_{II1} , as shown in Equations (12), (13), (17), and (18) and by their signs. A detailed comparison is shown in Figure 7 between the four elements, modifying the two angles θ_I

and θ_{II} and using the dimensions shown in Figure 6: $L_2 = 50$ mm, $a_{max} = b_{max} = 40$ mm, $D_A = 10$ mm, $D_B = 4$ mm, $a_i = b_i = [10, \dots, 40]^T$ mm.

In order to find the best configuration between the two mentioned above, the two force transformation matrices \mathbf{S}_{I0} and \mathbf{S}_{II0} (shown in Equations (11) and (16)) and their elements should be analysed. Using Equation (10), it is possible to write:

$$\Delta \mathbf{W} = \mathbf{W}_{P0} - \mathbf{W}_{P1} = \mathbf{S} \Delta \mathbf{T} \quad (21)$$

and then

$$\|\mathbf{S} \Delta \mathbf{T} - \Delta \mathbf{W}\|_2 = 0 \quad (22)$$

In order to obtain the minimum in the Equation (22), based on the properties of the norms and modifying only the matrix \mathbf{S} , we should have a minimum value of $\|\mathbf{S}\|_2$.

Unfortunately, \mathbf{S}_{I0} and \mathbf{S}_{II0} are rectangular matrices, and this aspect does not permit us to use simplifications for the square matrices. However, we used the singular value decomposition method [33] in order to find the singular values of the two matrices and to have an index on their characteristics. The singular values of \mathbf{S} are correlated to the eigenvalues of the matrix $\mathbf{S}^T \mathbf{S}$ and with the Euclidean norm of \mathbf{S} ($\|\mathbf{S}\|_2$). The following formulation is true:

$$\sigma_s(\mathbf{S}) = \sqrt{\lambda_s(\mathbf{S}^T \mathbf{S})} \quad (23)$$

$$\|\mathbf{S}\|_2 = \sigma_1(\mathbf{S}) \quad (24)$$

where σ_s and λ_s are the s singular values of \mathbf{S} and s eigenvalues of the matrix $\mathbf{S}^T \mathbf{S}$ ($s = 1, \dots, p$ and $\sigma_1 > \sigma_2 > \dots > \sigma_p \neq 0$); $\|\mathbf{S}\|_2$ is the Euclidean norm of \mathbf{S} ; and σ_1 the largest singular value of \mathbf{S} .

The following results have been found:

- The two matrices \mathbf{S}_{I0} and \mathbf{S}_{II0} have the same rank, equal to 5;
- $\|\mathbf{S}_{I0}\|_2 < \|\mathbf{S}_{II0}\|_2$.

To simplify the Equation (22), it is convenient to use configuration I with a smaller value of its Euclidean norm. However, configuration I has geometrical limitations with respect to configuration II. All cables in configuration I converge to the point O_B , and this limits the capacity of the structure to be fixed. Furthermore, the difference between two elements of the same configuration (h_{I0} , h_{II1} , or h_{II0} , h_{II1}) is smaller in configuration I compared to configuration II; this is shown in Figure 7. For these reasons, configuration II is selected as the best for our scope.

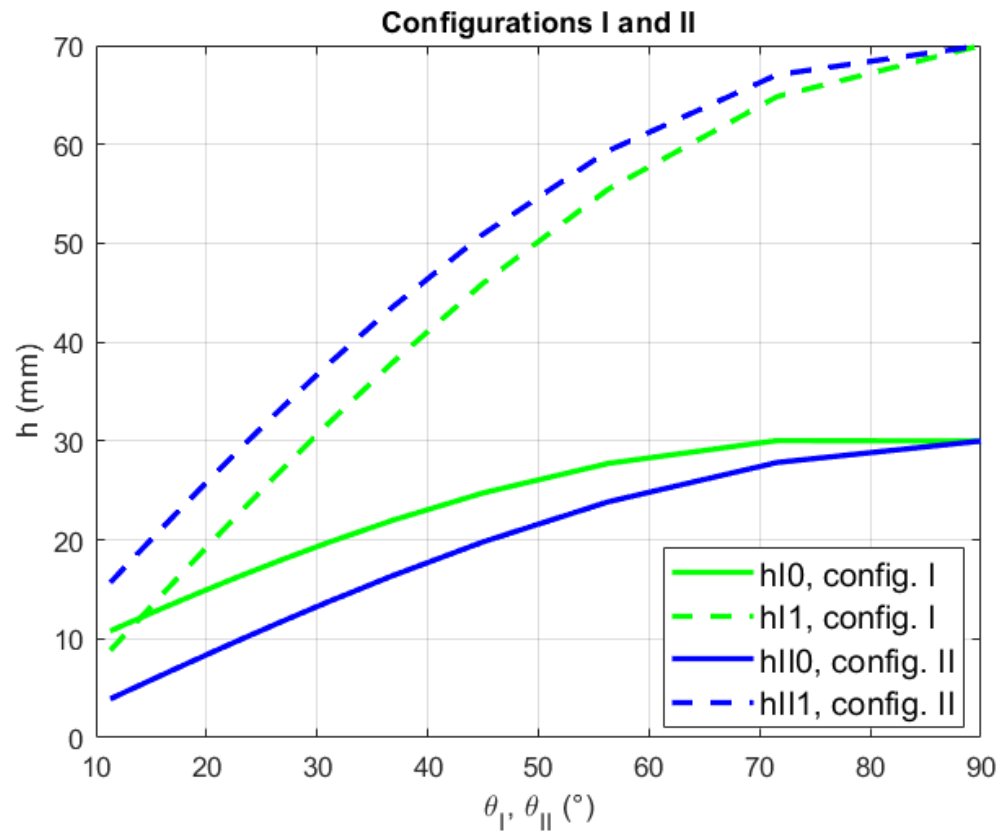


Figure 7. Comparison between the four h values (h_{10} , h_{11} , h_{110} , h_{111}) of the two matrices S_{10} and S_{110} .

5. Analytical Formulation of Configuration II

5.1. Force Transformation Matrix

The matrices S_{10} and S_{110} (found in Equations (11) and (16), respectively) are the simplified matrices for the two configurations in starting position (condition $j = 0$). Based on the analysis performed in previous sections, configuration II is the one recommended for our scope.

In order to use Equation (21) and to find the vector of the external forces and torques (W_{pj}), the force transformation matrix (S_{IIj}) and the vector of the variation in the tension of cables between the two conditions $j = 0$ and $j = 1$ (ΔT) must be calculated. In order to simplify the calculation, we used the model of configuration II shown in Figure 8, obtained with $a_i = 0$. In our case, $W_{p0} = 0$, and we can re-write Equation (10) it as:

$$W_{pj} = [F_{PX}, F_{PY}, F_{PZ}, M_{PX}, M_{PY}, M_{PZ}]^T = -S_{IIj} \Delta T \tag{25}$$

The new force transformation matrix S_{IIj} is:

$$S_{IIj} = \begin{bmatrix} S_{11j} & S_{12j} & S_{13j} & S_{14j} & S_{15j} & S_{16j} & S_{17j} & S_{18j} \\ S_{21j} & S_{22j} & S_{23j} & S_{24j} & S_{25j} & S_{26j} & S_{27j} & S_{28j} \\ S_{31j} & S_{32j} & S_{33j} & S_{34j} & S_{35j} & S_{36j} & S_{37j} & S_{38j} \\ S_{41j} & S_{42j} & S_{43j} & S_{44j} & S_{45j} & S_{46j} & S_{47j} & S_{48j} \\ S_{51j} & S_{52j} & S_{53j} & S_{54j} & S_{55j} & S_{56j} & S_{57j} & S_{58j} \\ S_{61j} & S_{62j} & S_{63j} & S_{64j} & S_{65j} & S_{66j} & S_{67j} & S_{68j} \end{bmatrix} \tag{26}$$

where the elements of the S_{IIj} matrix are shown in the following:

$$S_{11j} = -\sin(\alpha_{11})\cos(\gamma_b + \psi); S_{12j} = -\sin(\alpha_{21})\cos(\gamma_b + \psi); S_{13j} = \sin(\alpha_{31})\cos(\gamma_a); \quad (27)$$

$$S_{14j} = \sin(\alpha_{41})\cos(\gamma_a); S_{15j} = \sin(\alpha_{51})\sin(\gamma_c); S_{16j} = \sin(\alpha_{61})\sin(\gamma_c); \quad (28)$$

$$S_{17j} = \sin(\alpha_{71})\sin(\gamma_d + \psi); S_{18j} = \sin(\alpha_{81})\sin(\gamma_d + \psi); \quad (29)$$

$$S_{21j} = \sin(\alpha_{11})\sin(\gamma_b + \psi); S_{22j} = \sin(\alpha_{21})\sin(\gamma_b + \psi); S_{23j} = \sin(\alpha_{31})\sin(\gamma_a); \quad (30)$$

$$S_{24j} = \sin(\alpha_{41})\sin(\gamma_a); S_{25j} = \sin(\alpha_{51})\cos(\gamma_c); S_{26j} = \sin(\alpha_{61})\cos(\gamma_c); \quad (31)$$

$$S_{27j} = \sin(\alpha_{71})\cos(\gamma_d + \psi); S_{28j} = \sin(\alpha_{81})\cos(\gamma_d + \psi); \quad (32)$$

$$S_{31j} = -\cos(\alpha_{11}); S_{32j} = \cos(\alpha_{21}); S_{33j} = -\cos(\alpha_{31}); S_{34j} = \cos(\alpha_{41}); \quad (33)$$

$$S_{35j} = -\cos(\alpha_{51}); S_{36j} = \cos(\alpha_{61}); S_{37j} = -\cos(\alpha_{71}); S_{38j} = \cos(\alpha_{81}); \quad (34)$$

$$S_{41j} = C_{11}\sin(\alpha_{11})\sin(\gamma_b + \psi)\cos(\alpha_{11}); S_{42j} = -C_{21}\sin(\alpha_{21})\sin(\gamma_b + \psi)\cos(\alpha_{21}); \quad (35)$$

$$S_{43j} = C_{31}\sin(\alpha_{31})\sin(\gamma_a)\cos(\alpha_{31}); S_{44j} = -C_{41}\sin(\alpha_{41})\sin(\gamma_a)\cos(\alpha_{41}); \quad (36)$$

$$S_{45j} = C_{51}\sin(\alpha_{51})\cos(\gamma_c)\cos(\alpha_{51}); S_{46j} = -C_{61}\sin(\alpha_{61})\cos(\gamma_c)\cos(\alpha_{61}); \quad (37)$$

$$S_{47j} = C_{71}\sin(\alpha_{71})\cos(\gamma_d + \psi)\cos(\alpha_{71}); S_{48j} = -C_{81}\sin(\alpha_{81})\cos(\gamma_d + \psi)\cos(\alpha_{81}); \quad (38)$$

$$S_{51j} = -C_{11}\sin(\alpha_{11})\cos(\gamma_b + \psi)\cos(\alpha_{11}); S_{52j} = C_{21}\sin(\alpha_{21})\cos(\gamma_b + \psi)\cos(\alpha_{21}); \quad (39)$$

$$S_{53j} = C_{31}\sin(\alpha_{31})\cos(\gamma_a)\cos(\alpha_{31}); S_{54j} = -C_{41}\sin(\alpha_{41})\cos(\gamma_a)\cos(\alpha_{41}); \quad (40)$$

$$S_{55j} = C_{51}\sin(\alpha_{51})\sin(\gamma_c)\cos(\alpha_{51}); S_{56j} = -C_{61}\sin(\alpha_{61})\sin(\gamma_c)\cos(\alpha_{61}); \quad (41)$$

$$S_{57j} = C_{71}\sin(\alpha_{71})\sin(\gamma_d + \psi)\cos(\alpha_{71}); S_{58j} = -C_{81}\sin(\alpha_{81})\sin(\gamma_d + \psi)\cos(\alpha_{81}); \quad (42)$$

$$S_{61j} = S_{62j} = S_{63j} = S_{64j} = S_{65j} = S_{66j} = S_{67j} = S_{68j} = 0. \quad (43)$$

The terms of the elements of the S_{IIj} matrix are described below, with the help of Figures 8–10. Angle α_{ij} is the angle between the cable i (in the condition j) and the fixed central cylinder; C_{ij} is the length of the part of the cable i (in the condition j) between the two points N_{Aij} and N_{Bij} ; ψ is the angle that the component of the applied force in the XY plane has with respect to the Y_B axis; and $\gamma_a, \gamma_b, \gamma_c,$ and γ_d are the angles in the XY plane, formed by the cables as shown in the sketch of Figure 10, after displacement and rotation of the mobile reference system (centred in O_A), with respect to the absolute reference system (centred in O_B).

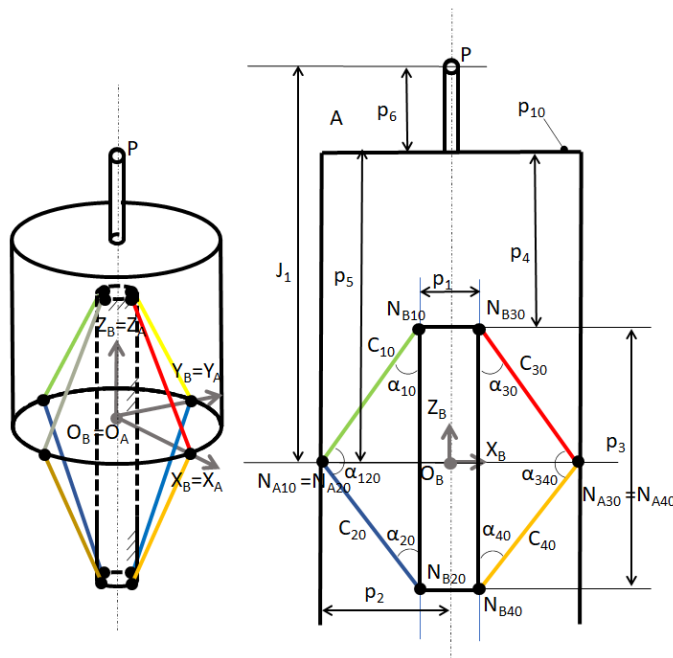


Figure 8. Trigonometric view (left) and planar XZ representation (right) of the architecture of the mechanism in $j = 0$ condition.

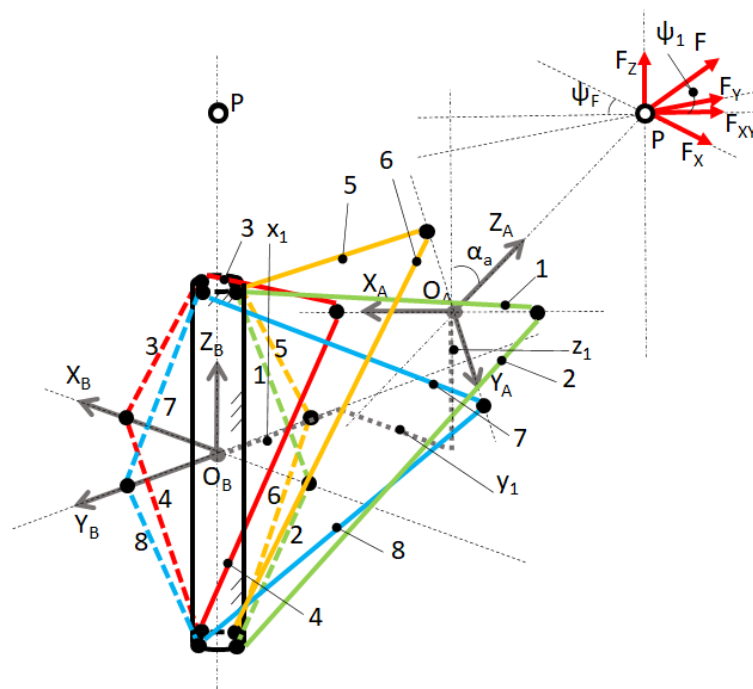


Figure 9. Sketch of the trigonometric view in translation and rotation of the local reference system (centred in O_A) with respect to the absolute reference system (centred in O_B). Displacement and rotation of $O_A - X_A Y_A Z_A$ are in the direction of the applied force F .

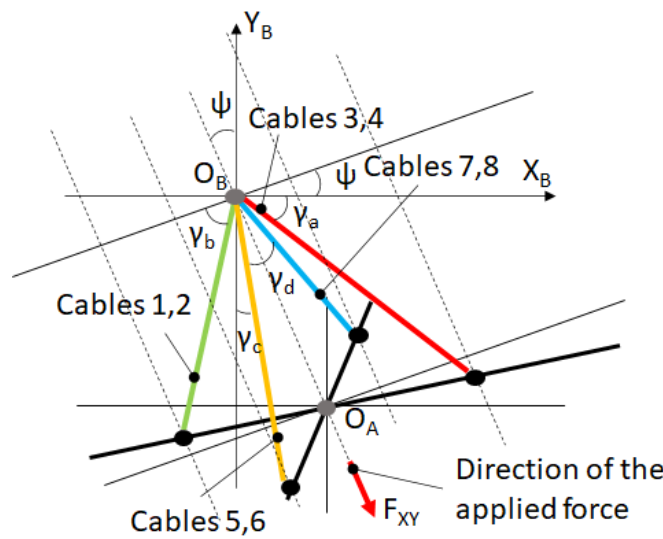


Figure 10. Sketch in the XY plane of the translation and rotation of the reference system centred in O_A with respect to the reference system centred in O_B . Displacement and rotation of $O_A - X_A Y_A Z_A$ are in the direction of the applied force F .

Using Carnot's theorem, the angle between two cables and the angle α_{ij} can be calculated as a function of the lengths p_3 and C_{ij} , shown in Figure 8, for the condition $j = 0$. In the following, this formulation is used to obtain α_{ij} :

$$\alpha_{121} = \arccos((C_{11}^2 + C_{21}^2 - p_3^2)/(2C_{11}C_{21})); \quad (44)$$

$$\alpha_{341} = \arccos((C_{31}^2 + C_{41}^2 - p_3^2)/(2C_{31}C_{41})); \quad (45)$$

$$\alpha_{561} = \arccos((C_{51}^2 + C_{61}^2 - p_3^2)/(2C_{51}C_{61})); \quad (46)$$

$$\alpha_{781} = \arccos((C_{71}^2 + C_{81}^2 - p_3^2)/(2C_{71}C_{81})); \quad (47)$$

$$\alpha_{11} = \arccos((p_3^2 + C_{11}^2 - C_{21}^2)/(2C_{11}p_3)); \quad (48)$$

$$\alpha_{21} = \arccos((p_3^2 + C_{21}^2 - C_{11}^2)/(2C_{21}p_3)); \quad (49)$$

$$\alpha_{31} = \arccos((p_3^2 + C_{31}^2 - C_{41}^2)/(2C_{31}p_3)); \quad (50)$$

$$\alpha_{41} = \arccos((p_3^2 + C_{41}^2 - C_{31}^2)/(2C_{41}p_3)); \quad (51)$$

$$\alpha_{51} = \arccos((p_3^2 + C_{51}^2 - C_{61}^2)/(2C_{51}p_3)); \quad (52)$$

$$\alpha_{61} = \arccos((p_3^2 + C_{61}^2 - C_{51}^2)/(2C_{61}p_3)); \quad (53)$$

$$\alpha_{71} = \arccos((p_3^2 + C_{71}^2 - C_{81}^2)/(2C_{71}p_3)); \quad (54)$$

$$\alpha_{81} = \arccos((p_3^2 + C_{81}^2 - C_{71}^2)/(2C_{81}p_3)). \quad (55)$$

With the obtained α_{ij} , the Z components of the length C_{ij} can be computed as a function of C_{ij} :

$$C_{11z} = -C_{11}\cos(\alpha_{11}); C_{21z} = C_{21}\cos(\alpha_{21}); C_{31z} = -C_{31}\cos(\alpha_{31}); C_{41z} = C_{41}\cos(\alpha_{41}); \quad (56)$$

$$C_{51z} = -C_{51}\cos(\alpha_{51}); C_{61z} = C_{61}\cos(\alpha_{61}); C_{71z} = -C_{71}\cos(\alpha_{71}); C_{81z} = C_{81}\cos(\alpha_{81}). \quad (57)$$

Then, the angles that $O_A - X_A Y_A Z_A$ forms with respect to $O_B - X_B Y_B Z_B$ in X (α_X) and Y (α_Y) are obtained, and ψ and α_A (shown in Figure 10) can be calculated.

$$\alpha_X = \arctan((|C_{5z} - C_{7z}|)/p_1); \alpha_Y = \arctan((|C_{3z} - C_{1z}|)/p_1); \quad (58)$$

$$\psi = \arctan((\tan(\alpha_Y))/(\tan(\alpha_X))); \quad (59)$$

$$\alpha_A = \arctan(\tan(\alpha_X)/\cos(\psi)) = \arctan(\tan(\alpha_Y)/\sin(\psi)). \quad (60)$$

In conclusion, the four angles $\gamma_a, \gamma_b, \gamma_c,$ and γ_d (shown in Figure 10) can be obtained as follows:

$$\gamma_a = \arccos((p_2\cos(\psi))/(C_{31}\sin(\alpha_{31}))) - \psi; \quad (61)$$

$$\gamma_b = \arccos((p_2\cos(\psi))/(C_{11}\sin(\alpha_{11}))); \quad (62)$$

$$\gamma_c = \arccos((p_2\cos(\pi/2 - \psi))/(C_{51}\sin(\alpha_{51}))) - \pi/2 + \psi; \quad (63)$$

$$\gamma_d = \pi/2 - \gamma_c - \arccos((p_2\sin(\psi))/(C_{71}\sin(\alpha_{71}))). \quad (64)$$

Using the formulations in the previous equations, the X and Y components of the C_{ij} are obtained:

$$C_{11x} = -C_{11}\sin(\alpha_{11})\cos(\gamma_b + \psi); C_{11y} = -C_{11}\sin(\alpha_{11})\sin(\gamma_b + \psi); \quad (65)$$

$$C_{21x} = C_{11x}; C_{21y} = C_{11y}; C_{31x} = C_{31}\sin(\alpha_{31})\cos(\gamma_a); \quad (66)$$

$$C_{31y} = -C_{31}\sin(\alpha_{31})\sin(\gamma_a); C_{41x} = C_{31x}; C_{41y} = C_{31y}; \quad (67)$$

$$C_{51x} = C_{51}\sin(\alpha_{51})\sin(\gamma_c); C_{51y} = -C_{51}\sin(\alpha_{51})\cos(\gamma_c); \quad (68)$$

$$C_{61x} = C_{51x}; C_{61y} = C_{51y}; C_{71x} = C_{71}\sin(\alpha_{71})\sin(\gamma_d + \gamma_c); \quad (69)$$

$$C_{71y} = -C_{71}\sin(\alpha_{71})\cos(\gamma_d + \gamma_c); C_{81x} = C_{71x}; C_{81y} = C_{71y}. \quad (70)$$

Now, it is possible to compute the displacement of the centre of the mobile system O_A (x_1, y_1, z_1) and of the point P (x_P, y_P, z_P) of the applied external forces:

$$x_1 = |C_{31x}| - |C_{11x}|; y_1 = |C_{71y}| - |C_{51y}|; \tag{71}$$

$$z_1 = p_3/2 - (|C_{51z}| + |C_{71z}| + |C_{31z}| + |C_{11z}|)/4. \tag{72}$$

$$x_P = x_1 + J_1 \sin(\alpha_Y); y_P = y_1 + J_1 \sin(\alpha_X); z_P = z_1 - J_1(1 - \cos(\alpha_A)) + J_3. \tag{73}$$

5.2. Vector of the Cable's Tension

All formulations shown in the last sub-section are functions of the cable's length C_{ij} , computed with the following equations.

In our proposed idea, the cables are supposed to be non-extensible. Figure 11 (left) shows a planar sketch of the behaviour of the entire sensor in the two conditions (e.g., $j = 0$ and $j = 1$). Each cable is connected with a spring with a stiffness coefficient k_i . The variation in the length C_{ij} is a function of the displacement in each spring of the sensor:

$$\Delta C_{i10} = \Delta L_{mi10}; \Delta C_{i10} = C_{i1} - C_{i0}; \Delta L_{mi10} = L_{mi1} - L_{mi0}; \tag{74}$$

$$C_{i1} = C_{i0} + L_{mi1} - L_{mi0}. \tag{75}$$

In Equation (75), the cable's length in the condition $j = 1$ is obtained. L_{mi1} is the difference between the length of the spring i (in the condition j) and its initial length. The values of C_{ij} in the initial conditions ($j = 0$) are obtained as follows:

$$C_{10} = C_{20} = C_{30} = C_{40} = C_{50} = C_{60} = C_{70} = C_{80} = \sqrt{(p_3/2)^2 + (p_2)^2}; \tag{76}$$

$$\alpha_{10} = \alpha_{20} = \alpha_{30} = \alpha_{40} = \alpha_{50} = \alpha_{60} = \alpha_{70} = \alpha_{80} = \arctan(p_3/2p_2). \tag{77}$$

Using the same approach, it is possible to calculate the ideal cable tension near the spring in the two conditions T_{i1m} and T_{i0m} :

$$T_{i1m} = k_i L_{mi1}; T_{i0m} = k_i L_{mi0}; \Delta T_{i10m} = T_{i1m} - T_{i0m}. \tag{78}$$

Figure 11 (right) shows the tensions of cables 1 and 2. Based on the forces shown in the picture, the cable's tension near the mobile part (T_{11p} or T_{21p}) is function of the force of the spring (T_{11m} or T_{21m}).

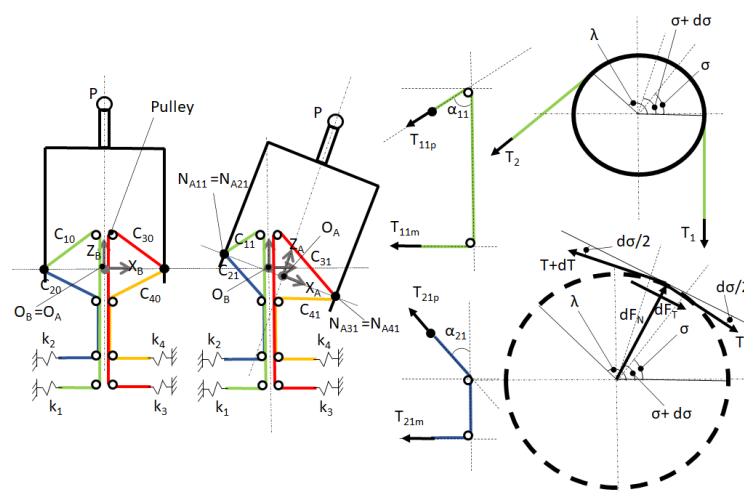


Figure 11. Planar sketch of the behaviour of the sensitive mechanism in the two conditions ($j = 0$ and $j = 1$) (left) and example of the calculation of the cable's tension in cables 1 and 2 (right). Each cable is considered inextensible, and the motion of the condition $j = 1$ is possible thanks to the displacement of the springs: k_1, k_2, k_3, k_4 .

In order to calculate the cables' tension on the mobile part, the following formulations can be obtained for cables 1 and 2. μ is the friction coefficient between the cable and the pulley. If the pulley is fixed, the cable crawls on the cylindrical surface of the pulley. This is the case analysed in this paper.

$$(T + dT)\cos(d\sigma/2) - T\cos(d\sigma/2) - dF_T = 0; \quad (79)$$

$$dF_N - (T + dT)\sin(d\sigma/2) - T\sin(d\sigma/2) = 0. \quad (80)$$

$$\cos(d\sigma/2) \approx 1; \sin(d\sigma/2) \approx d\sigma/2; \quad (81)$$

$$dT = dF_T; dF_N - Td\sigma = 0; dF_T = \mu dF_N; \mu Td\sigma = dT; \quad (82)$$

$$T_2 = T_1 e^{\mu\lambda}. \quad (83)$$

$$T_{11p} = T_{11m} e^{\mu(3\pi/2 - \alpha_{11})}; T_{21p} = T_{21m} e^{\mu(\pi/2 + \alpha_{21})}; T_{31p} = T_{31m} e^{\mu(3\pi/2 - \alpha_{31})}; \quad (84)$$

$$T_{41p} = T_{41m} e^{\mu(\pi/2 + \alpha_{41})}; T_{51p} = T_{51m} e^{\mu(3\pi/2 - \alpha_{51})}; T_{61p} = T_{61m} e^{\mu(\pi/2 + \alpha_{61})}; \quad (85)$$

$$T_{71p} = T_{71m} e^{\mu(3\pi/2 - \alpha_{71})}; T_{81p} = T_{81m} e^{\mu(\pi/2 + \alpha_{81})}; \quad (86)$$

$$T_{10p} = T_{10m} e^{\mu(3\pi/2 - \alpha_{10})}; T_{20p} = T_{20m} e^{\mu(\pi/2 + \alpha_{20})}; T_{30p} = T_{30m} e^{\mu(3\pi/2 - \alpha_{30})}; \quad (87)$$

$$T_{40p} = T_{40m} e^{\mu(\pi/2 + \alpha_{40})}; T_{50p} = T_{50m} e^{\mu(3\pi/2 - \alpha_{50})}; T_{60p} = T_{60m} e^{\mu(\pi/2 + \alpha_{60})}; \quad (88)$$

$$T_{70p} = T_{70m} e^{\mu(3\pi/2 - \alpha_{70})}; T_{80p} = T_{80m} e^{\mu(\pi/2 + \alpha_{80})}; \quad (89)$$

The general equation can be obtained as follows:

If $i = 1, 3, 5, 7$:

$$T_{ijp} = T_{ijm} e^{\mu(3\pi/2 - \alpha_{ij})}; \quad (90)$$

If $i = 2, 4, 6, 8$:

$$T_{ijp} = T_{ijm} e^{\mu(\pi/2 + \alpha_{ij})}. \quad (91)$$

The vector of the cable tension can be obtained using the following equation:

$$\Delta T_{1p} = T_{11p} - T_{10p}; \Delta T_{2p} = T_{21p} - T_{20p}; \Delta T_{3p} = T_{31p} - T_{30p}; \Delta T_{4p} = T_{41p} - T_{40p}; \quad (92)$$

$$\Delta T_{5p} = T_{51p} - T_{50p}; \Delta T_{6p} = T_{61p} - T_{60p}; \Delta T_{7p} = T_{71p} - T_{70p}; \Delta T_{8p} = T_{81p} - T_{80p}. \quad (93)$$

$$\Delta \mathbf{T}_p = [\Delta T_{1p} \Delta T_{2p} \Delta T_{3p} \Delta T_{4p} \Delta T_{5p} \Delta T_{6p} \Delta T_{7p} \Delta T_{8p}]^T. \quad (94)$$

The final equation to consider in order to find the external forces and torques is:

$$\mathbf{W}_p = -\mathbf{S}_{IIj} \Delta \mathbf{T}_p. \quad (95)$$

6. Model Validation and Physical Implementation with Two Test Bench Prototypes

6.1. Model Validation

In order to test how much the physical dimensions of the mechanism and the friction on the cables influence the proposed model, we decided to test our model in two test benches of different dimensions of the mechanism and with different levels of cable friction. Our basic idea is that if our model gives good answers in different dimensions of the mechanism, this would confirm the feasibility of recreating our system in reduced dimensions and its ability to be used (in the near future) inside a surgical instrument of a maximum diameter of 10 mm. Test bench I (TBI) is the bigger and planar mechanism. Test bench II (TBII) is the smaller spatial mechanism. The dimensions of the two test benches used are shown in Table 1.

Table 1. Dimensions of the test bench prototypes. Measures ($p_1, p_2, p_3, p_4, p_6, p_{10}$) are shown in Figure 8.

	p_1 (mm)	p_2 (mm)	p_3 (mm)	p_4 (mm)	p_6 (mm)	p_{10} (mm)	μ
TBI	23	85	100	43	7	82	0
TBII	16	8.75	13.5	11.8	12	2.5	0.3; 0.25 [34]

6.2. Planar Test Bench Prototype: TBI

Figure 12 shows the scheme of TBI, and Figure 13 shows the prototype developed to validate and implement the proposed cable-driven mechanism. In TBI, we analysed the planar application using four cables. Part B is fixed and part A is the mobile part. Pulleys are attached to part B, and four cables connect part A with part B. Four springs are connected to the four cables, and thanks to their movements, the motion of point P is found. Another cable connects the applied load to point P. The spherical joints are attached between the mobile part A and the planar base (fixed plane) in order to enable the motion of part A in the plane, reducing friction. The pulleys in the Figure 13 are used to validate the behaviour of the mechanism without friction acting on the cables.

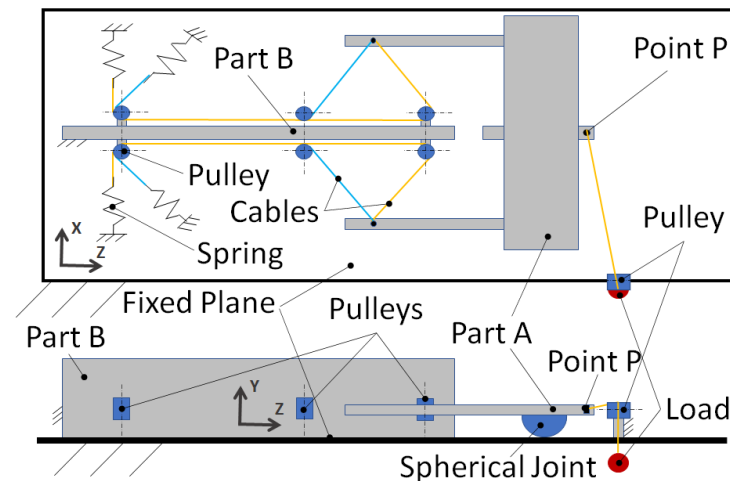


Figure 12. Scheme of the planar test bench prototype (TBI) to study the behaviour of the sensitive mechanism.

6.3. Spatial Test Bench Prototype: TBII

Figure 14 shows the TBII prototype realized with a 3D printer and used to study the sensing mechanism. Part A is the mobile part consisting of a hollow cylinder with radial holes for the cable connections and a central shaft for the application of the external forces. Part B consists of a central shaft and an external hollow cylinder fixed on a plane. Part B includes holes that facilitate the connection with the cables. Part A is assembled on the central shaft of part B, in its zone with a minimum diameter. A planar section is shown in Figure 14 with cables 5, 6, 7, 8 and stiffness coefficients k_5, k_6, k_7, k_8 . Two cable blocks are used to fix cables 6 and 5 and cables 8 and 7 to part A. The motion of part A can be evaluated using the displacement of the springs.

Figure 15 shows the TBII used for the experiments. An external force F is applied in the YZ plane, modifying the cables' tension. Measuring the displacement of the springs allows us to find the displacement of the point of the applied force F , and thanks to Equation (94), the vector of the cables' tension (ΔT_p) is computed. Using Equation (95), the external forces and torques are measured.

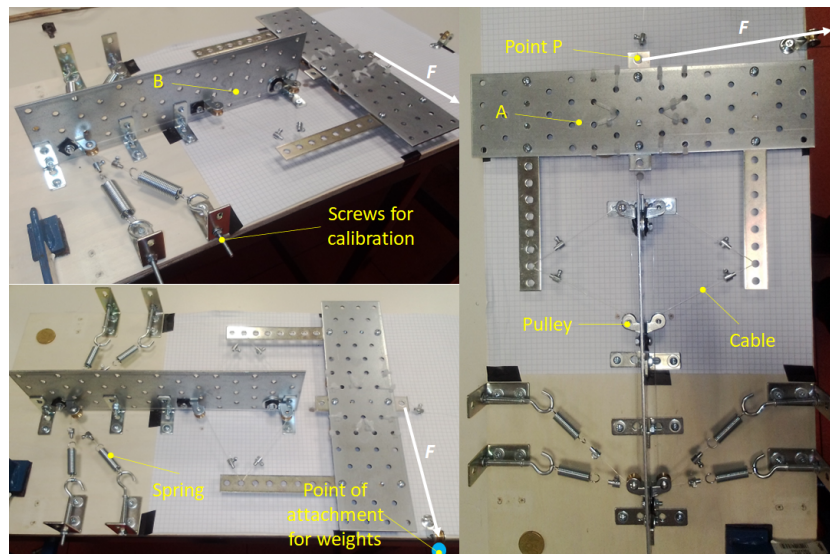


Figure 13. Planar test bench prototype (TBI) to study the behaviour of the sensitive mechanism. A is the mobile part and B is the fixed part.

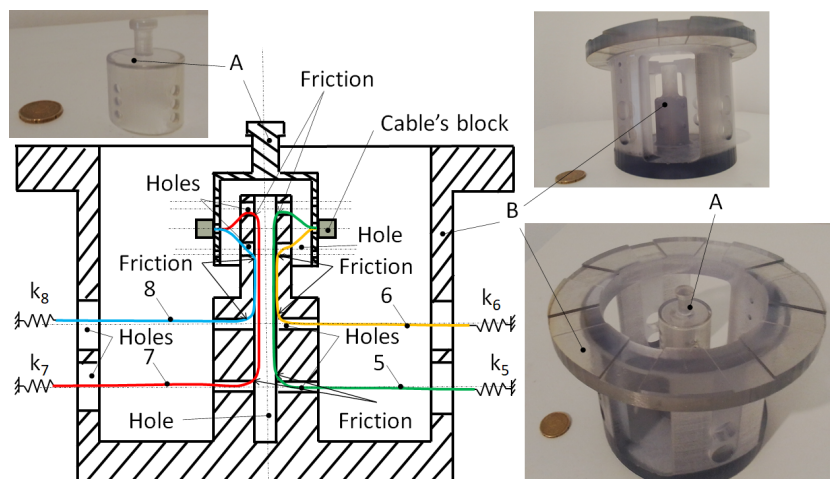


Figure 14. Spatial test bench prototype (TBII) to study the behaviour of the sensing mechanism: section with cables inside the test bench; realized prototype (with a 3D printer) of parts A (mobile part) and B (fixed part).

6.4. Springs and Cables

In order to test the sensitive mechanism, we tried many types of cables and springs, and in the following, we will show only the selection used in the experiments. The material of the cable is nylon, with a diameter of 0.6 mm. The dimensions of the spring used in the experiments are shown in Table 2. The stiffness coefficient of the spring is calculated by applying a load (after a preload condition) and measuring the displacement of the spring obtained with the applied load.

Table 2. Dimensions of the type of spring used in the experiment: D_e is the external diameter; d is the diameter of the wire; L_m is the initial length of the spring; n is the number of wraps; k is the stiffness coefficient.

	D_e (mm)	d (mm)	L_m (mm)	n	k (N/mm)
Spring	9.4	1	24.8	25	0.6786

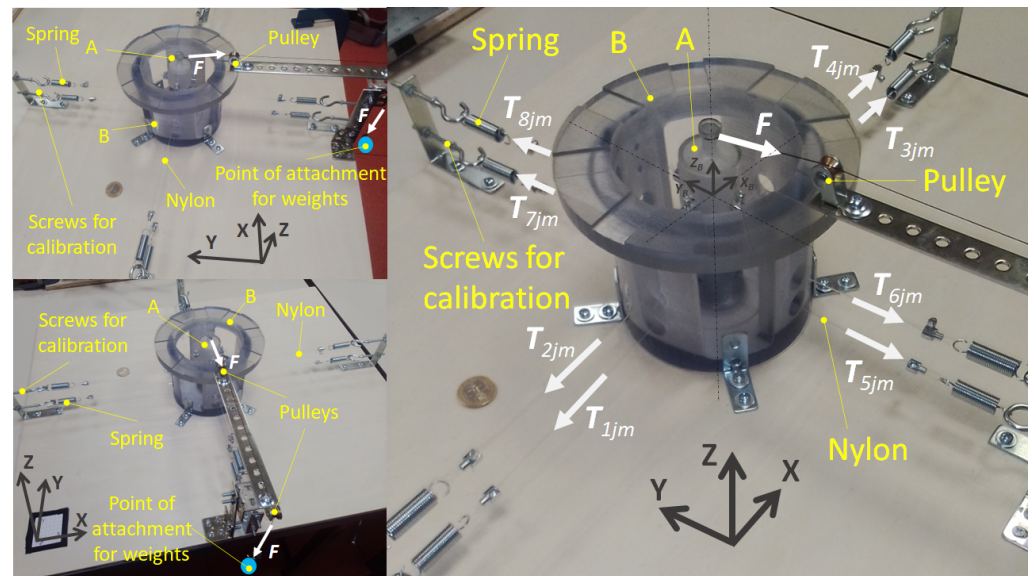


Figure 15. Experiments with the TBII for the behavioural analysis of the sensitive mechanism: external applied force F and eight cables' tensions: T_{1jm} , T_{2jm} , T_{3jm} , T_{4jm} , T_{5jm} , T_{6jm} , T_{7jm} , T_{8jm} . A is the mobile part and B is the fixed part.

The springs are connected between the cable and external fixed connections. Manual calibration of the cable tension is performed on the external connections using screws.

6.5. Implementation

Part B of the test bench prototype is fixed on a plane using screws. Part A is connected to part B, as described in the previous sections. In the first step, we attached the nylon cable to part A, after passing the cables through part B (in the pulleys of TBI or in the holes of TBII). An external force F is applied on part A, as shown in Figures 13 and 15. Force is created by adding different weights to the point of attachment for the weights, shown in Figures 13 and 15. In each experiment using TBI or TBII, we performed the same process, described as follows:

- 1 Attachment of the spring to the cable;
- 2 Attachment of the spring to the fixed part;
- 3 Centring of part A and calibration using screws in the fixed part;
- 4 Measuring the spring's length in the condition $j = 0$;
- 5 Applying weights to the point of attachment for the weights;
- 6 Measuring the spring's length in the condition $j = 1$.

In each test (TBI and TBII), we applied loads in the sequence shown in Table 3.

Table 3. Sequence of the Applied Loads.

	1 (N)	2 (N)	3 (N)	4 (N)	5 (N)	6 (N)	7 (N)
TBI	6.46	7.48	8.49	9.85	10.94		
TBII	3.25	4.26	5.27	6.46	7.48	8.49	9.57

Using the formulations shown in the previous sections, we considered only the positive cable tension values in order to transfer the information to the software that the cable is only able to pull and not to push.

7. Comparison between Measured and Calculated Forces: Results and Discussion

7.1. Results

In following, the results of the comparison between measured and calculated forces on the point P are shown. By using formulations shown in the last sections, the values shown in Tables 1–3 and Figures 16 and 17 are obtained. The black points represent the measured applied loads on point P; the blue points represent the points computed using the following formulation (96) to calculate the applied resultant forces:

$$F_{\text{calculated}} = \sqrt{F_X^2 + F_Y^2 + F_Z^2}. \quad (96)$$

where F_X , F_Y , and F_Z are the first three elements of the vector \mathbf{W}_{pj} .

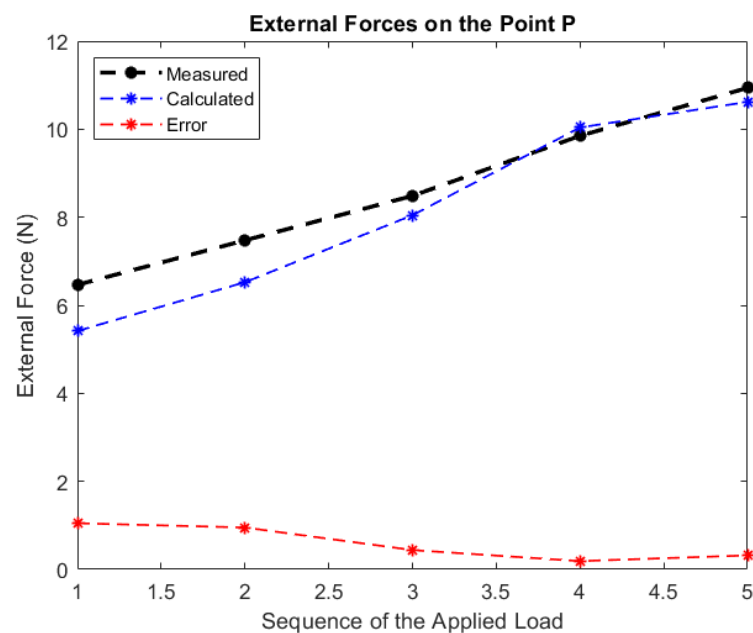


Figure 16. TBI: Comparison between measured and calculated external forces on the point P. The error is obtained by the absolute difference between measured and calculated values of the force.

7.2. Discussion

Figure 16 shows the comparison between measured and computed external forces on the point P if the planar TBI is used. Figure 17 shows the same situation in which TBII is used. In TBI, it seems that if the sequence of load increases, the error is reduced. A different behaviour is noted in TBII, in which the error seems to have a more constant behaviour, maybe influenced by the friction.

In TBII, it is possible to note a maximum absolute error of around 0.64 N and a minimum error of around 0.03 N if the friction coefficient $\mu = 0.25$ is used. The mean of all errors obtained for the seven loads are around 0.33 N. In case of using $\mu = 0.3$, the maximum absolute error is around 2 N, and a minimum error is around 0.13 N. The mean of all errors noted in each applied load is around 1.13 N. In conclusion, in TBII, the maximum percentage of relative error to calculate the external force is around 28% if $\mu = 0.3$ is used, and 9% if $\mu = 0.25$ is used. The absolute error is calculated as the difference between the measured and calculated value of the force (or displacement). The percentage of the relative error is calculated as the ratio between the absolute error and the measured value multiplied by 100.

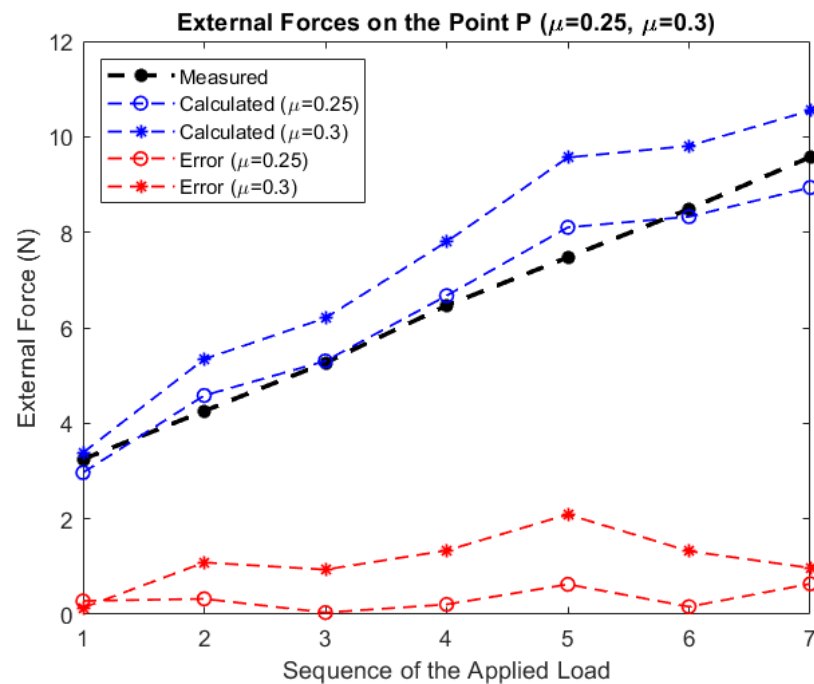


Figure 17. TBII: Comparison between measured and calculated external forces on the point P using two different values of friction: $\mu = 0.25$ and $\mu = 0.3$ [34]. The error is obtained by the absolute difference between measured and calculated values of the force.

Based on the obtained results, it is important to underline that this is a first test of these prototypes, and two points of contact between each cable and the part B are present in TBI and TBII. This generates many errors, because no pulley is used in TBII. However, the model presented in this paper gives the same behaviour of the forces in the two different test bench prototypes. This is a very good initial result and opens new possibilities for future developments of the mechanism.

8. Conclusions

In this paper, we present a new cable-driven model of an under-actuated sensing mechanism for robotic surgery and micro/macro applications, where the under-actuation is a fundamental aspect of the design. The proposed mechanism is conceived with an under-actuated system with cables and could solve the big problem of sterilization in robotic surgery, permitting the use of electronic parts in surgical instruments while avoiding their sterilization. This paper presents the first results of the implementation of the proposed model in two test bench prototypes of different dimensions. Future works are oriented toward realizing another spatial test bench with reduced dimensions and to perform other tests with digital sensors for comparison. We would like to reduce the dimensions of the test bench of the mechanism in order to implement the model in a prototype of a 10 mm diameter, which will be directly mounted on the robotic surgery tool. Furthermore, we will try to reduce friction, including pulleys, in the spatial test bench.

Author Contributions: Conceptualization, G.G.M.; methodology, G.G.M. and P.F.; software, G.G.M.; validation, G.G.M. and P.F.; formal analysis, G.G.M.; investigation, G.G.M.; resources, P.F.; data curation, G.G.M.; writing—original draft preparation, G.G.M.; writing—review and editing, G.G.M. and P.F.; visualization, G.G.M. and P.F.; supervision, G.G.M. and P.F.; project administration, G.G.M. and P.F.; funding acquisition, P.F. All authors have read and agreed to the published version of the manuscript.

Funding: This work was supported in part by the European Union Grants ERC-ADG N. 742671 and ARS (Autonomous Robotic Surgery) project. URL: <https://www.ars-project.eu>, (accessed on 23 April 2023).

Data Availability Statement: Not applicable.

Conflicts of Interest: The authors declare no conflict of interest.

Abbreviations

The following abbreviations are used in this manuscript:

CDPR	cable-driven parallel robots
dVRT	da Vinci Robotic Tool
MIRS	Minimally Invasive Robotic Surgery
dVRA	da Vinci Robotic Arm
MIRT	Minimally Invasive Robotic Tool
dVRK	da Vinci Robotic Kit
E-E	End-Effector
TBI	Test Bench I
TBII	Test Bench II

References

- Muscolo, G.G.; Fiorini, P. force–torque Sensors for Minimally Invasive Surgery Robotic Tools: An overview. *IEEE Trans. Med. Robot. Bionics* **2023**. [[CrossRef](#)]
- Zhang, T.; Gong, X.; Zhang, L.; Wang, Y.; Liu, Y.; Li, L. A Method for Solving the Additional Stiffness Introduced by Flexible Joints in Stewart Platform Based on FEM Modal Analysis. *Machines* **2023**, *11*, 457. [[CrossRef](#)]
- Dasgupta, B.; Mruthyunjaya, T. The Stewart platform manipulator: A review. *Mech. Mach. Theory* **2000**, *35*, 15–40. [[CrossRef](#)]
- Sorli, M.; Pastorelli, S. Six-axis reticulated structure force/torque sensor with adaptable performances. *Mechatronics* **1995**, *5*, 585–601. [[CrossRef](#)]
- Ranganath, R.; Nair, P.S.; Mruthyunjaya, T.S.; Ghosal, A. A force–torque sensor based on a Stewart Platform in a near-singular configuration. *Mech. Mach. Theory* **2004**, *39*, 971–998. [[CrossRef](#)]
- Kübler, B.; Seibold, U.; Hirzinger, G. Development of actuated and sensor integrated forceps for minimally invasive robotic surger. *Int. J. Med. Robot. Comput. Assist. Surg.* **2005**, *1*, 96–107. [[CrossRef](#)]
- Dai, J.S.; Kerr, D.R. A six-component contact force measurement device based on the Stewart platform. *Proc. Inst. Mech. Eng. Part C J. Mech. Eng. Sci.* **2000**, *214*, 687–697. [[CrossRef](#)]
- Chao, L.P.; Chen, K.T. Shape optimal design and force sensitivity evaluation of six-axis force sensors. *Sens. Actuators A Phys.* **1997**, *63*, 105–112. [[CrossRef](#)]
- Muscolo, G.; Recchiuto, C.; Molino, R. Dynamic balance optimization in biped robots: Physical modeling, implementation and tests using an innovative formula. *Robotica* **2015**, *33*, 2083–2099. [[CrossRef](#)]
- Zhou, S.; Sun, J.; Gao, F. Influence of flexible spherical joints parameters on accuracy of the six-axis force/torque sensor with three-three orthogonal parallel mechanism. *Mech. Mach. Theory* **2020**, *145*, 103697. [[CrossRef](#)]
- Zhenlin, J.; Feng, G.; Xiaohui, Z. Design and analysis of a novel isotropic six-component force/torque sensor. *Sens. Actuators A Phys.* **2003**, *109*, 17–20. [[CrossRef](#)]
- Kim, J.H.; Kang, D.I.; Shin, H.H.; Park, Y.K. Design and analysis of a column type multi-component force/moment sensor. *Measurement* **2003**, *33*, 213–219. [[CrossRef](#)]
- Franchi, V.; Di Rito, G.; Galatolo, R.; Cannella, F.; Caldwell, D.; Muscolo, G.G. Modelling and control design of a novel robotic membrane. *Int. J. Mech. Control* **2019**, *20*, 113–122.
- Franchi, V.; Di Rito, G.; Galatolo, R.; Cannella, F.; Caldwell, D.; Muscolo, G.G. Multibody Analysis and Design of an Electromechanical System Simulating Hyperelastic Membranes. In *Multibody Dynamics 2019, ECCOMAS 2019; Computational Methods in Applied Sciences; Kecskeméthy, A., Geu Flores, F., Eds.; Springer: Cham, Switzerland, 2020; Volume 53*.
- Mannella, D.; Bellusci, M.; Graziani, F.; Ferraresi, C.; Muscolo, G.G. Modelling, design and control of a new seat-cushion for pressure ulcers prevention. *Proc. Inst. Mech. Eng. Part H J. Eng. Med.* **2022**, *236*, 592–602. [[CrossRef](#)] [[PubMed](#)]
- Bottero, S.; Muscolo, G.G.; Ferraresi, C. A New Soft RCC Device with Pneumatic Regulation. *Robotics* **2020**, *9*, 98. [[CrossRef](#)]
- Muscolo, G.G.; Fontana, M. A novel linear pneumatic actuator with tunable-compliance constraint. *Int. J. Mech. Control* **2020**, *21*, 73–86.
- Xiong, H.; Diao, X. A review of cable-driven rehabilitation devices. *Disabil. Rehabil. Assist. Technol.* **2020**, *15*, 885–897. [[CrossRef](#)]
- Paterna, M.; Magnetti, G.; De Benedictis, C.; Muscolo, G.G.; Ferraresi, C. A passive upper-limb exoskeleton for industrial application based on pneumatic artificial muscles. *Mech. Sci.* **2022**, *13*, 387–398. [[CrossRef](#)]

20. Pott, A.; Mütterich, H.; Kraus, W.; Schmidt, V.; Miermeister, P.; Verl, A. IPAnema: A family of Cable-Driven Parallel Robots for Industrial Applications. In *Cable-Driven Parallel Robots; Mechanisms and Machine Science*; Bruckmann, T., Pott, A., Eds.; Springer: Berlin/Heidelberg, Germany, 2013; Volume 12.
21. Cheng, Y.; Ren, G.; Dai, S. The multi-body system modelling of the Gough–Stewart platform for vibration control. *J. Sound Vib.* **2004**, *271*, 599–614. [[CrossRef](#)]
22. Gosselin, C. Cable-driven parallel mechanisms: State of the art and perspectives. *Mech. Eng. Rev.* **2014**, *1*, DSM0004. [[CrossRef](#)]
23. Piao, J.; Kim, E.S.; Choi, H.; Moon, C.B.; Choi, E.; Park, J.O.; Kim, C.S. Indirect force control of a cable-driven parallel robot: Tension estimation using artificial neural network trained by force sensor measurements. *Sensors* **2019**, *19*, 2520. [[CrossRef](#)] [[PubMed](#)]
24. Müller, M.S.; Hoffmann, L.; Christopher, Buck, T.; Walter Koch, A. Fiber Bragg grating-based force–torque sensor with six degrees of freedom. *Int. J. Optomechatron.* **2009**, *3*, 201–214. [[CrossRef](#)]
25. He, C.; Wang, S.; Sang, H.; Li, J.; Zhang, L. Force sensing of multiple-DOF cable-driven instruments for minimally invasive robotic surgery. *Int. J. Med. Robot. Comput. Assist. Surg.* **2014**, *10*, 314–324. [[CrossRef](#)] [[PubMed](#)]
26. Chen, Q.; Lin, Q.; Wei, G.; Ren, L. Tension vector and structure matrix associated force sensitivity of a 6-DOF cable-driven parallel robot. *Proc. Inst. Mech. Eng. Part C J. Mech. Eng. Sci.* **2022**, *236*, 100–114. [[CrossRef](#)]
27. Shimachi, S.; Hirunyanitiwatna, S.; Fujiwara, Y.; Hashimoto, A.; Hakozaiki, Y. Adapter for contact force sensing of the da Vinci[®] robot. *Int. J. Med. Robot. Comput. Assist. Surg.* **2008**, *4*, 121–130. [[CrossRef](#)]
28. Moradi Dalv, M.; Shirinzadeh, B.; Shamdani, A.H.; Smith, J.; Zhong, Y. An actuated force feedback-enabled laparoscopic instrument for robotic-assisted surgery. *Int. J. Med. Robot. Comput. Assist. Surg.* **2014**, *10*, 11–21. [[CrossRef](#)]
29. Wang, Z.; Wang, D.; Chen, B.; Yu, L.; Qian, J.; Zi, B. A clamping force estimation method based on a joint torque disturbance observer using PSO-BPNN for cable-driven surgical robot end-effectors. *Sensors* **2019**, *19*, 5291. [[CrossRef](#)]
30. Sang, H.; Yun, J.; Monfaredi, R.; Wilson, E.; Fooladi, H.; Cleary, K. External force estimation and implementation in robotically assisted minimally invasive surgery. *Int. J. Med. Robot. Comput. Assist. Surg.* **2017**, *13*, e1824. [[CrossRef](#)]
31. Shi, C.; Lai, D.; Tang, Z.; Yang, Z. Development of an optic fiber-based torque sensor with a torsion-translation conversion flexure. *IEEE Sens. J.* **2021**, *22*, 344–351. [[CrossRef](#)]
32. Kim, U.; Kim, Y.B.; So, J.; Seok, D.Y.; Choi, H.R. Sensorized surgical forceps for robotic-assisted minimally invasive surgery. *IEEE Trans. Ind. Electron.* **2018**, *65*, 9604–9613. [[CrossRef](#)]
33. Klema, V.; Laub, A. The singular value decomposition: Its computation and some applications. *IEEE Trans. Autom. Control* **1980**, *25*, 164–176. [[CrossRef](#)]
34. Shooter, K.V.; Tabor, D. The frictional properties of plastics. *Proc. Phys. Soc. Sect. B* **1952**, *65*, 661. [[CrossRef](#)]

Disclaimer/Publisher’s Note: The statements, opinions and data contained in all publications are solely those of the individual author(s) and contributor(s) and not of MDPI and/or the editor(s). MDPI and/or the editor(s) disclaim responsibility for any injury to people or property resulting from any ideas, methods, instructions or products referred to in the content.